Numerical simulation of irradiation hardening in Zirconium

A. Boyne [a], C. Shen [c], R. Najafabadi [b], Y. Wang [a,*]

[a] Dept. Mat. Sci. Eng., Ohio State University, 2041 N. College Road, Columbus, OH 43221, United States
[b] Knolls Atomic Power Laboratory, 2401 River Road, Schenectady, NY 12309, United States
[c] GE Global Research, 1 Research Circle, Schenectady, NY 12309, United States

ARTICLE INFO

ABSTRACT

A phase field model is developed to simulate interactions between gliding dislocations and irradiation induced damage loops (i.e., vacancy and self-interstitial loops) in Zirconium. Pinning contact interactions and long-range elastic interactions are simulated, with populations of defects generated based on experimental observations of typical damage microstructures in irradiated Zr. The model is employed to simulate irradiation hardening as a function of damage loop density. We find that the stress fields of damage loops contribute significantly to their effective obstacle strength, and that the elastic interactions cause the dependence of critical resolved shear stress on damage loop number density to deviate from analytical predictions of dispersed barrier hardening. The simulation predictions of the yield strength agree well with experimental measurements for different damage loop densities.

© 2013 Elsevier B.V. All rights reserved.

1. Introduction

Reduced ductility due to irradiation hardening is a common problem in the Zirconium based alloys that are often used as fuel cladding tubes in pressurized water reactors [1–3]. Irradiation damage in pure Zr or Zr-alloys is characterized by the formation of populations of vacancy and interstitial loops (herein referred to as "damage loops"). Damage loops are dislocation loops with $\langle a \rangle$-type Burgers vectors, having habit planes distributed between the $\{11\bar{2}0\}$ planes and the adjacent $\{10\bar{1}0\}$ planes. The number density (N) of the loops increases with increasing fluence and exposure time, until it eventually saturates at a maximum level [1,4,5]. Values of N reported in the literature average around 2×10^{22} m^{-3}, with a maximum reported near 6×10^{22} m^{-3} [2–8]. The damage loops are elliptical in shape and are sometimes observed to align in layers, parallel to the basal plane [1,9]. Some $\langle c \rangle$ type damage loops have also been observed, but $\langle a \rangle$ type loops are by far the most numerous [1,10].

Concurrent with the development of damage loops, Zr-alloys undergo a marked increase in yield strength [5,11–17]. The hardening depends on dose, exposure time, and test conditions, but typically an increment of roughly 100 MPa is observed in the yield stress when tested at room temperature [16,17]). It is one of the primary undesirable outcomes of irradiation in Zr-based alloys [5,12,14,16,18].

Irradiation hardening in Zr has previously been analyzed via the Dispersed Barrier Hardening (DBH) theory [8,16,18,19]. DBH theory posits that the hardening is produced by the action of irradiation-induced defects as point obstacles (i.e. Orowan obstacles) to dislocation glide [19]. This theory may be contrasted with, for instance, cascade-induced source hardening, in which radiation defects are assumed to decorate grown-in dislocations and provide a barrier to the initiation of glide [20]. DBH has been assumed in the specific case of Zr, owing to the condensed nature of the damage loops [14,16].

Analytical expressions of irradiation hardening derived from DBH theory have the following form:

$$\Delta\tau = \alpha\mu b\sqrt{Nd} \tag{1}$$

where $\Delta\tau$ is the increment in critical resolved shear stress, α is a constant term proportional to the pinning strength of irradiation induced obstacles, μ is the shear modulus, b is the magnitude of the Burgers vector, N is the number density of obstacles and d is the average diameter of obstacles [21]. The average spacing of a randomly spatially distributed population of Orowan obstacles is typically approximated by $(Nd)^{-\frac{1}{2}}$, the effective square lattice spacing [22]. Expressions of this form have been used to interpret and predict hardening of irradiated materials including Zr [18,21,23–25]. For damage loops, an α value of approximately 0.5 has been employed [21]. This simple model has often been used as a component of a more sophisticated crystal plasticity model (e.g. [14,24]).

The analytical expression of dispersed barrier hardening relies on the accuracy of regular spacing approximations and the

* Corresponding author.
  E-mail address: wang.363@osu.edu (Y. Wang).

assumption that only Orowan hardening is active. Simple computational models of obstacle hardening have been used for several decades to document the effect of spatial non-uniformity on obstacle hardening [26,27]. Foreman and Makin developed the first line-tracking model to investigate hardening by randomly distributed obstacles. Subsequently, their work has been widely adopted and refined, particularly in the context of oxide dispersion strengthening, to produce a number of similar line tracking models [26,28–32] It has also informed obstacle hardening simulations using the Discrete Dislocation Dynamics (DDD) method [33–36]. These line-tracking models have been used to investigate the effects of random spatial distribution of obstacles, random distribution of obstacle shape and strength, and elastic interaction between segments of the gliding dislocation. As a result, scalar corrections for elastic interaction and random spatial distribution have been developed, while rules of mixture have been validated for distributions of obstacle shape and strength. It is also important to note that these simulations in general do not consider the clearing of obstacles by gliding dislocations [37,38]. Hardening obstacles – particularly obstacles such as forest dislocations and damage loops – may be cleared by gliding dislocations with sufficient applied stress [37,38]. This results in the formation of "channels" which are cleared of obstacles; these channels in turn result in significant localization of plastic deformation and are an important feature of the overall plastic response of irradiated materials [13,18]. Simulations which neglect this mechanism will thus necessarily overestimate the actual yield strength increment which would be observed in real materials.

Li et al. have studied irradiation hardening in steels via a DDD model, incorporating the stress fields of damage loops via analytical solutions [39]. Jumel et al. and Adjanor et al. performed line-tracking simulations of irradiation hardening in steels but approximated irradiation induced defects as point obstacles, and neglected long-range elastic interaction between damage loops and dislocations [35,36]. Nogaret et al. have studied interactions between dislocations and Frank loops in detail via a nanoscale DDD model, focusing on the mechanism of formation of cleared bands [37]. Several authors have studied the nature of irradiation defects and their interaction with dislocations in irradiated metals at an atomistic scale [37,40–48]. While such simulations are critical in understanding the nature and strength of individual irradiation-induced obstacles, they are limited in time and length scales.

In this paper we propose a computational model employing the phase field method to study irradiation hardening in pure Zr due to the presence of damage loops. As compared to line-tracking methods, the phase field approach is attractive in that it provides the capability to eventually consider arbitrary dislocation reactions as well as the time-evolution of irradiation induced defects (e.g. growth or dissolution) in a single, self-consistent framework. In particular, we study dislocation interactions with a static population of defects, representative of typical irradiation damage in Zr alloys. The long range elastic interaction fields of arbitrary configurations of loops are calculated via the Khachaturyan–Shatalov phase field microelasticity theory [49]. Short range or contact interactions between loops and glide dislocations are treated as discrete obstacles, based on a simplified analysis of possible interaction types in the irradiated Zr system. We construct representative populations of damage loops and simulate dislocation glide through them, measuring the minimum required stress for a dislocation to pass through (the critical resolved shear stress, CRSS). Long-range elastic interactions between damage loops and dislocations are found to produce a hardening effect that is complementary to hardening due to contact interactions, and that affects the trend of hardening with respect to damage loop density. Hardening values predicted by our model are then compared with experimental measurements, and good agreement is found.

2. Methodology

2.1. Phase field formulation

We describe the interaction of a gliding dislocation with damage loops via the phase field microelasticity theory of dislocations, wherein dislocation glide is represented by the motion of local inelastic deformation fields. Our model consists of two sets of field variables: $\{\phi\}$, representing the damage loops, and $\{\eta\}$ representing the glide dislocation. The total free energy functional of the system is

$$E^{total} = E^{total}[\{\eta\}, \{\phi\}]$$
$$= \int d\vec{r}[f(\{\eta(\vec{r}), \phi(\vec{r})\}) + \kappa|\nabla\{\eta(\vec{r}), \phi(\vec{r})\}|^2]$$
$$+ \int \frac{d\vec{k}}{(2\pi)^3}\left[C_{ijkl}\epsilon_{ij}^T(\vec{k})\epsilon_{kl}^{T^*}(\vec{k}) - n_i\sigma_{ij}^T(\vec{k})\Omega_{jk}(\vec{n})\sigma_{kl}^{T^*}(\vec{k})n_l\right] \quad (2)$$

The first integral in Eq. (2) includes the energy contributions from local interaction (the crystalline energy, f) and short-range spatial correlation (the gradient term). The second integral, formulated in the reciprocal space, gives the strain energy from long range elastic interactions [49]. The local eigenstrain field $\epsilon_{ij}^T(\vec{r})$ is given by

$$\epsilon_{ij}^T(\vec{r}) = \sum_p \epsilon_{ij}^{T0}(p)\eta_p(\vec{r}) + \sum_q \epsilon_{ij}^{T0}(q)\phi_q(\vec{r}) \quad (3)$$

where p and q label the slip systems of the glide dislocation and damage loops respectively, and ϵ_{ij}^{T0} is the stress-free transformation strain of a dislocation, given by [50]

$$\epsilon_{ij}^{T0}(\eta_p) = \frac{(\vec{n}_p \otimes \vec{b}_p + \vec{b}_p \otimes \vec{n}_p)}{2d_p} \quad (4)$$

Here $\vec{n}_p$, $\vec{b}_p$ and d_p are the slip plane normal vector, Burgers vector, and inter-slip plane distance of the pth slip system respectively, and $\otimes$ is the dyadic product. Eq. (4) applies to both glide dislocations and damage loops. The remaining variables in the second integral of Eq. (2) are: $\sigma_{ij}^T = C_{ijkl}\epsilon_{kl}^T$, $[\Omega^{-1}]_{jk} = n_i C_{ijkl}n_l$, $\vec{k}$ is a vector in the reciprocal space, and $\vec{n} = \vec{k}/|\vec{k}|$.

In our simulations, we have made the simplifying assumption that the damage loops are completely sessile. Damage loops are actually glissile in their Burgers vector direction, and thus able to move in response to local or external forces. There is also the possibility of movement by climb (e.g. damage loop coarsening during irradiation). In principle it would be straightforward to include these processes within the phase field model. However, considering damage loop motion necessitates a large increase in computational time. Given this assumption that only the glide dislocation fields will evolve, we need only expand the terms in the first integral of Eq. (2) with respect to η. So long as the crystalline and gradient energy forms are properly chosen, the phase field model has the capability to capture the evolution and reaction of dislocation networks on an arbitrary number of slip planes.

The crystalline energy is a state function of the local inelastic deformation, which is in turn characterized by the local eigenstrain tensor field [51]

$$f = f(\{\eta\}) = f\left(\sum_p \epsilon_{ij}^{T0}(p)\eta_p(\vec{r})\right) \quad (5)$$

If the active slip systems share a common slip plane, the local inelastic deformation reduces to a simple shear parallel to the plane. In this case, f can be written as [52]

$$f = \frac{\gamma(\vec{u})}{d} \quad (6)$$

where γ is the generalized stacking fault (GSF) energy [53], $\vec{u} = \sum_p \vec{b}_p \eta_p(\vec{r})$, and d is the interplanar spacing. The GSF energy may be calculated using the *ab initio* method, allowing for quantitative study of dislocation cores as well as dissociated (partial) dislocations in arbitrary geometries in a phase field framework. In this work, since we will consider a single active slip system, the GSF is approximated by

$$\gamma = \gamma(\eta) = \left(\frac{c_{66}b^2}{2\pi^2 d}\right)\sin^2(\pi\eta) \tag{7}$$

In the phase field dislocation model, a general form of the gradient energy is given as [50]

$$\kappa|\nabla\{\eta\}|^2 \equiv \sum_{p,p'}(\vec{\beta}_{pp'})_{ijkl}\frac{\partial(\vec{b}_p)_i}{\partial r_j}\frac{\partial(\vec{b}_{p'})_k}{\partial r_l} \tag{8}$$

where $\vec{\beta}_{pp'}$ is a coefficient tensor. A particular convenient form of Eq. (8) is given in [51]

$$\sum_{p,p'}\xi_{pp'}\frac{\vec{b}_p \cdot \vec{b}_{p'}}{b_p b_{p'}}(\vec{n}_p \times \nabla\eta_p) \cdot (\vec{n}_{p'} \times \nabla\eta_{p'}) \tag{9}$$

which automatically satisfies Frank's rule of Burgers vector sum. The coefficient matrix $\xi_{pp'}$ simplifies to a scalar constant if the slip systems p and p' are crystallographically equivalent.

Dislocation glide is described by the evolution of η, which is governed by a time-dependent Ginzburg–Landau type equation [50]:

$$\frac{\partial\eta(\vec{r},t)}{\partial t} = -L\frac{\delta E^{total}}{\delta\eta(\vec{r},t)} \tag{10}$$

which assumes a linear dependence of the rate of change of η on the variation of total energy with respect to η. L is a kinetic parameter, proportional to dislocation mobility.

2.2. Contact interaction with damage loops

We now discuss the treatment of contact interactions between damage loops and glide dislocations. Long-range elastic interactions are considered automatically via the second integral in Eq. (2), but short range interactions will require an additional mechanism. First, we must consider the nature of these interactions in terms of the geometrical character of the active dislocation slip systems. As was mentioned above, damage loops have $\langle a \rangle$ type Burgers vectors [10]. It has also been established that the dominant active slip system in pure Zr is the prismatic system, with glide dislocations having $\vec{b} = \frac{a}{3}\langle 11\bar{2}0 \rangle$ and gliding on the $\{10\bar{1}0\}$ planes [54]. Thus, for any given prismatic glide plane there will be three distinct relative orientations of damage loops: one with Burgers vector in the plane (and equal to that of the glide dislocation), and two with Burgers vectors tilted out of the plane. For convenience these three damage loop orientations will be numbered as $\langle a_i \rangle$ where $i = 1 \ldots 3$, as shown in Fig. 1. While damage loop normals are distributed between the $\langle 10\bar{1}0 \rangle$ and $\langle 11\bar{2}0 \rangle$ directions, we will make the assumption that they are uniformly along the $\langle 10\bar{1}0 \rangle$ direction adjacent to their $\vec{b}$. Furthermore, it has been established that slip in pure Zr is controlled by the much slower screw dislocations [54]. Consequently, all simulated glide dislocations will have an initially screw character.

Pinning interactions between intersecting dislocations have been extensively studied, due to their importance in controlling hardening and other important aspects of plasticity. Several types of interactions are possible, depending on the character of the dislocations, including the formation of unit steps or jogs [55,56],
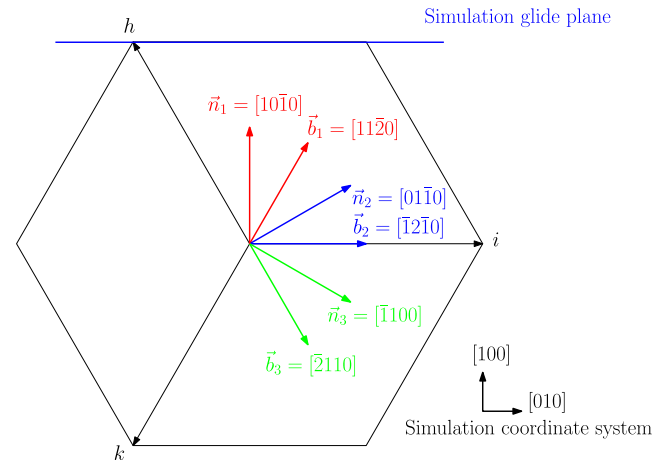

Fig. 1. Schematic of the conventional HCP unit cell, showing the principal relative directions of damage loop $\vec{b}$ and $\vec{n}$ considered in our analysis. The prismatic glide plane of the simulation is shown as a horizontal blue line at the top, while the coordinate axes of the simulation are shown at the bottom right. For clarity, only three unique relative orientations have been illustrated above; in reality, both negative orientations and slight deviations of the normal vectors are possible. (For interpretation of the references to colour in this figure legend, the reader is referred to the web version of this article.)

reactions [55,57], and the formation of attractive junctions [58]. A unit step is a step equal in magnitude and direction to the respective $\vec{b}$ of the intersecting dislocations, which may or may not be sessile with respect to glide (and thus pinning) depending on the specifics of dislocations character. While the formation of unit jogs has been previously proposed as a hardening mechanism in interactions with prismatic loops in hexagonal crystals [56], subsequent work suggests that the formation of attractive junctions is nearly always the most important pinning mechanism [58]. Onimus et al. have recently conducted a detailed study of damage loop and gliding dislocation interactions specifically in irradiated Zr-alloys, combining *in situ* TEM observations with theoretical analysis of contact interactions [59].

Junction formation is driven primarily by attractive, short-range elastic interactions between out-of-plane dislocations; a reduction in the total energy of the two dislocations can be achieved by the formation of a third, sessile segment at the point of intersection – a junction. This process has been shown to be dominant in strain or forest-obstacle hardening [58,60,61], and is thus likely to be the dominant hardening mechanism in the interaction between prismatic loops and gliding screw dislocations. An accurate and complete understanding of the hardening process in irradiated Zr alloys will necessarily build on a detailed atomistic analysis of the formation and strength of junctions between all of the most likely dislocation/damage loop configurations. However, it is certain that point intersections at damage loops act as strong obstacles to glide in irradiated Zr alloys [14,18,59].

In these simulations, we propose to treat these interactions as discrete obstacles to dislocation motion in the glide plane. Specifically, we will make the assumption that sessile contact interactions may be treated as small, unshearable obstacles to glide (essentially, Orowan obstacles). It has been shown that attractive junctions produce hardening consistent with the Orowan mechanism, with an additional scaling factor accounting for the distribution of pinning strengths associated with the population of interactions Madec et al. [58]. In the absence of a detailed catalog of such interaction strengths, we will simplify the general problem to a more tractable limiting case: the assumption of infinite junction strength, which necessitates clearance by Orowan looping. Treating junctions between damage loops and gliding prismatic

dislocations in this manner will therefore consistently overestimate their strength. An additional simplification implicit in the above description is the lack of loop clearing or annihilation mechanisms. The channel clearing mechanism which we describe above is consistently observed in irradiated Zr alloys with loop populations which undergo plastic deformation Onimus et al. [13,14,62]. By asssuming perfect obstacle strength and a static loop population, we implicitly neglect the potential for loop clearing and channel-formation. We make this assumption for simplicity (and some potential avenues for relaxing it will be discussed in the Section 4.4), but it must be emphasized that this also contributes to an overestimation of the hardening effect of damage loops. We will restrict subsequent analysis of our results to the impact on initial yield strength, before significant plastic deformation has taken place, specifically in order to minimize the impact of these simplifications on our conclusions.

Referring again to Fig. 1 and our assumptions regarding damage loop normals and $\vec{b}$, we judge that interaction with $\langle a_2 \rangle$-type damage loops will result in absorption of the loop and the formation of a helix [37,55]. Because we neglect loop clearing, we will assume that interactions with $\langle a_2 \rangle$-type damage loops will be purely mediated by long-range elastic interactions. Since this is not the case in both $\langle a_1 \rangle$ and $\langle a_3 \rangle$ loops, they will potentially form attractive junctions with gliding dislocations at their points of intersection with the glide plane. However, we have assumed that $\langle a_1 \rangle$ damage loops have their normals coincident with the normal of the simulated glide plane – i.e. they will either be entirely contained within the glide plane, or fall entirely outside of it. This means that calculating a singular point of intersection is not possible, and intersection would be extremely rare in any case. Consequently, only the intersection points of $\langle a_3 \rangle$-type damage loops will be considered as additional obstacles (that is, beyond long-range elastic interactions, which are considered for all loop-types).

Since we treat the damage loops as sessile, the locations of intersection between the glide plane and damage loops which would be pinning for the slip system being considered are predetermined. At these locations, an un-shearable particle is placed whose diameter is equal to the width of the diffuse dislocation core. Practically, this is implemented via the mobility coefficient L in Eq. (10). Instead of a constant, we make L a position dependent field $L(\vec{r})$, such that $L(\vec{r}) = 0$ when $\vec{r}$ is within a jog "particle". When a glide dislocation encounters a jog "particle", it will behave in a manner analogous to Orowan looping. We employ the approximate model described above in order to capture the hardening effect of damage loops beyond that produced by long-range elastic interactions. As described above, the results of this model are necessarily an overestimate of the hardening effect due to damage loops. It does not explicitly consider the formation of sessile junctions, but rather models their impact on glide dislocations via the limiting case of infinite obstacle strength for certain static configurations. Nonetheless, it provides a simple avenue for the investigation of the details of the hardening process, which may be expanded on in future work.

Hardening is measured via the critical resolved shear stress (CRSS), using the following algorithm. A dislocation is placed at the edge of a computational cell containing a given population of damage loops, which will act as obstacles via their long-range elastic interaction fields and the formation of pinning jogs. Shear stress is applied with a magnitude just sufficient to produce the free glide of an unobstructed dislocation. A continuous test of the instantaneous strain rate (where strain is measured by the percentage of area slipped) is made; if the dislocation is pinned (i.e. the strain rate goes to zero), then the applied stress in increased. This is repeated until the applied stress is sufficient to allow the dislocation to overcome all the obstacles in the glide plane, and the ultimate magnitude is reported as the CRSS.

3. Results

3.1. Simulation parameters

We consider a single active slip system: the prismatic $(10\bar{1}0)$ plane, with Burgers vector $\vec{b} = [1\bar{2}10]$. For brevity, we designate the three damage loop types as: $\langle a_1 \rangle$ with $\vec{b} = [\bar{2}110]$, $\langle a_2 \rangle$ with $\vec{b} = [\bar{1}2\bar{1}0]$, and $\langle a_3 \rangle$ with $\vec{b} = [11\bar{2}0]$. A rectilinear coordinate system is used for the simulations, with the following axes: $x = [10\bar{1}0]$, $y = [1\bar{2}10]$, and $z = [0001]$. These are chosen for convenience such that the glide plane lies on the YZ plane. All simulations use the elastic constants: $c_{11} = c_{22} = 144$ GPa, $c_{33} = 165$ GPa, $c_{12} = 72.5$ GPa, $c_{13} = c_{23} = 65$. 4 GPa, $c_{44} = c_{55} = 32.1$ GPa, and $c_{66} = 35.5$ GPa [63]. The governing equation was numerically solved with a fully explicit spectral technique, with a Δt of 0.01, a gradient coefficient ξ of 0.8, and the grid length normalized to the length of a glide dislocation Burgers vector. An inherent lattice friction stress develops in the phase field simulation due to the spatial discretization of the computational cell, which is analogous of Peierl's stress – a minimum stress necessary for glide. This was characterized for our model via 1 dimensional simulations in the absence of damage loops, and for the parameter set used here it was found to be approximately 14.2 MPa, similar to values reported in atomistic simulations in Zr [64].

Recall that two out of three damage loop types have habit planes which are inclined with respect to the glide plane. Given the coordinate system described above, these loop types will lie on non-rational planes. Since our simulation employs a square grid, it is not possible to accurately resolve these damage loops with one grid (one $\vec{b}$) thickness – in order to prevent artifacts the thickness of these damage loops was increased artificially by at least a factor of three. Consequently, we scale the ϵ_{ij}^{T0} by a factor of one third in order to avoid increasing the magnitude of the long-range elastic interaction. The accuracy of this approximation was verified by comparison with analytical expressions for the dislocation stress field.

3.2. Regular arrays

First, we consider the CRSS of regular arrays of damage loops. A single damage loop is placed in the center of a computational cell ($256 \times 512 \times$ NZ grid points in size); the stress field and location of any pinning points due to the presence of the loop is pre-calculated. Since periodic boundary conditions are employed, this configuration effectively corresponds to a regular periodic array of damage loops, with a lateral spacing equal to NZ. The CRSS of such regular arrays of obstacles has been treated extensively in the literature [65], and thus serves as a point of comparison and validation for our model.

If we neglect the stress field of the damage loops, then we recover the classical Orowan hardening case for $\langle a_3 \rangle$ damage loops (see Fig. 2). The CRSS results for this case are reported and compared with analytical predictions (using Eq. (1) with $\sqrt{Nd}$ replaced with L^{-1} to recover the classic Orowan relation) in Table 1. We find good agreement between the two trends, with our model predicting $\alpha = 0.79$ when least-squares fit to the Orowan equation ($\alpha \approx 0.8$ has been predicted for unshearable obstacles when considering self-elastic interaction of the glide dislocation [65]).

When the stress fields of the damage loops are considered, we find the results summarized in Table 2. All of these simulations were conducted with the damage loop placed 5 grids (appx. 1.5 nm) below the glide plane. Compared to pinning from contact interactions alone, the addition of long-range elastic interactions to a pinning jog increases hardening and produces a CRSS vs. spacing curve which fits to $\alpha = 1.17$.
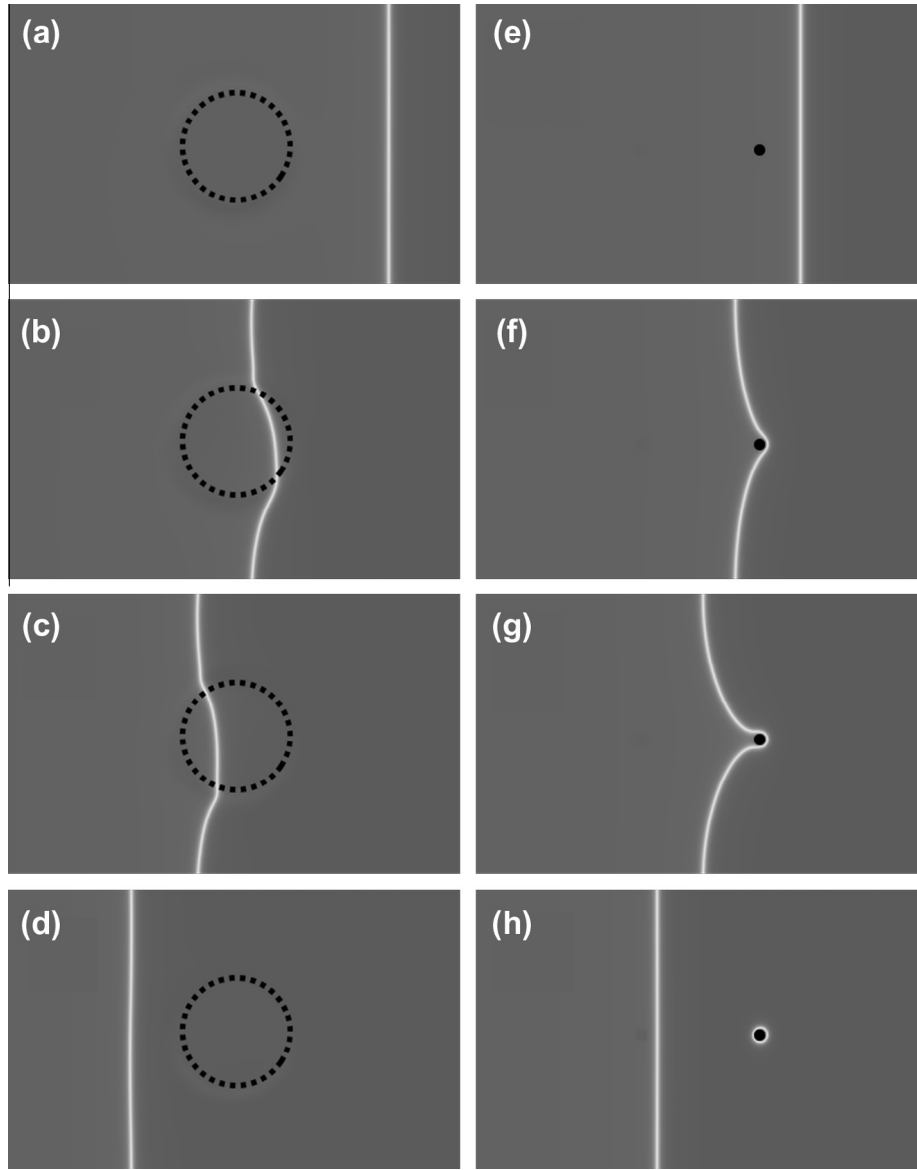
Fig. 2. Sequential snapshots of dislocation evolution when encountering a single strong elastic obstacle (left, a–d) and a single pinning jog (right, e–h). The elastic obstacle was produced by an $\langle a_1 \rangle$ damage loop placed 1.4 nm below the glide plane, while the pinning jog was simply placed *ad hoc* in the center of the glide plane, without any associated stress field.

Table 1
CRSS as a function of obstacle spacing for a simulation without long-range elastic interactions. L is the obstacle spacing determined by the simulation dimensions. The DBH column was calculated as $\alpha \mu \, bL^{-1}$, with $\alpha = 0.79$.

L (nm)	CRSS (MPa)	
	This work	DBH
8.74	908.8	872.3
17.47	418.9	436.1
34.94	205.9	218.1

Table 2
Summary of the effect of long-range elastic interaction on CRSS. L is the obstacle spacing determined by the simulation dimensions.

L (nm)	CRSS (MPa)			
	Junction $+ \langle a_3 \rangle$	$\langle a_3 \rangle$	$\langle a_2 \rangle$	$\langle a_1 \rangle$
8.74	1288.7	280.5	152.7	280.5
17.47	688.7	205.9	145.6	209.5
34.94	362.1	113.6	78.1	113.6

Pure elastic interaction, without any contact interactions, produces a hardening effect of magnitude lower than that of pure contact interaction (see Fig. 2). We find that the CRSS is nearly identical for $\langle a_1 \rangle$ and $\langle a_3 \rangle$ loops and is lowest for the $\langle a_2 \rangle$ loop simulations. In order to rationalize this, we examine the elastic interaction energy density fields of a typical damage loop. Elastic interaction energy density characterizes the net effect of the stress field of a damage loop on dislocation glide – positive values are repulsive (inhibit glide), while negative values are attractive (promote glide), and it is written as [66]:

$$e_{int}^{elast}(\vec{r}) = - \int_V \sigma_{ij}(\eta_p(\vec{r})) \epsilon_{ij}^o(\eta_q(\vec{r}')) dr^3$$

When resolved on a prismatic glide plane the field of a damage loop has a two-lobed profile, with one attractive and one repulsive locus (see Figs. 3 and 4). $\langle a_2 \rangle$ loops have a nearly symmetric

attractive/repulsive profile on the glide plane, while the other loop types are biased towards one lobe due to their tilt. Due to this symmetry the net resolved magnitude of an $\langle a_2 \rangle$ loop's elastic interaction field is lower than that of either $\langle a_1 \rangle$ or $\langle a_3 \rangle$ loop types when they are placed in a square array, and thus $\langle a_2 \rangle$ loops produce a smaller hardening effect. Additionally, $\langle a_1 \rangle$ and $\langle a_3 \rangle$ loops produce elastic interaction fields that are almost identical on the glide plane, which explains their equivalent hardening effects. These observations are strongly dependent on the orientation and position of the damage loop relative to the glide plane.
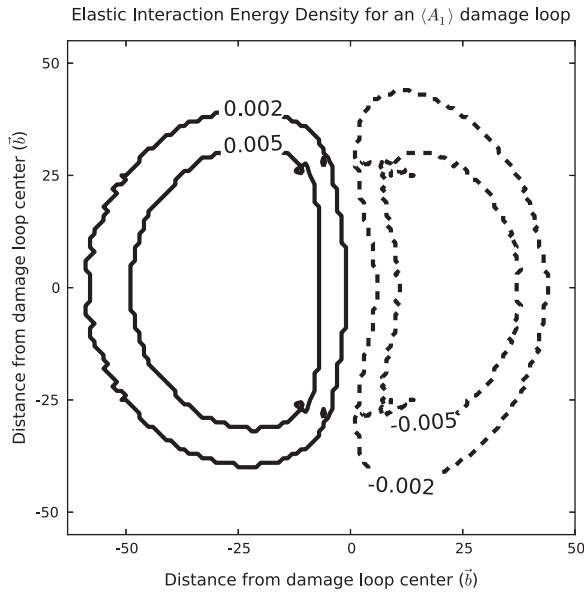
3.3. Random arrays

In order to study the effect of variation in loop size and non-uniform spatial distribution, simulations were performed with statistical variation of loop size, loop types and spatial distribution. Populations of damage loops were constructed in the following manner. We designate a desired number density and distributions of damage loop size, loop type and relative spatial orientation. A random number generator is then employed to produce a loop population having the desired characteristics, placing damage loops in a computational cell with dimensions 256 by 512 grids. Using the resultant ϕ_q fields, elastic interaction energy and pinning locations are calculated, and resolved onto the glide plane (an arbitrary YZ-slice of the computational cell, taken consistently at NX/2 in this work). We consider four levels of damage loop number density N: 1×10^{22} m^{-3}, 2×10^{22} m^{-3}, 4×10^{22} m^{-3}, and 6×10^{22} m^{-3}. These were chosen based on average values reported in the literature. Loops are evenly distributed between all three Burgers vectors, with an average radius of 10 nm, ±5 nm (randomly distributed).

Fig. 3. Contour plot of the elastic interaction energy density field of an $\langle a_1 \rangle$ damage loop, resolved on the glide plane. This slice was taken approximately 7 nm above the center of the damage loop (along *X*-axis direction).
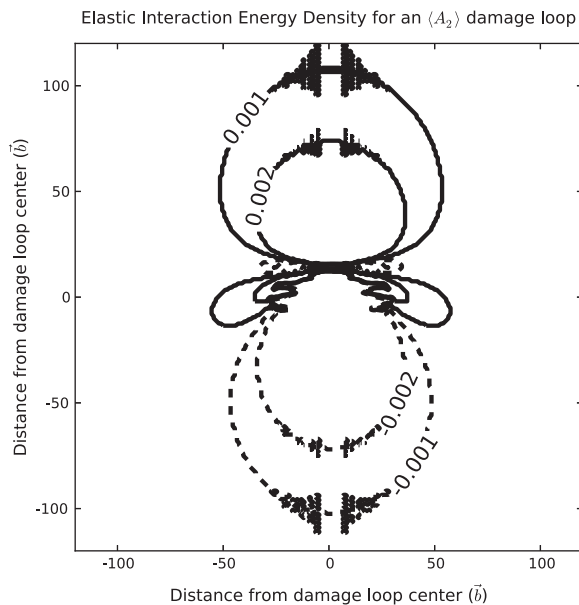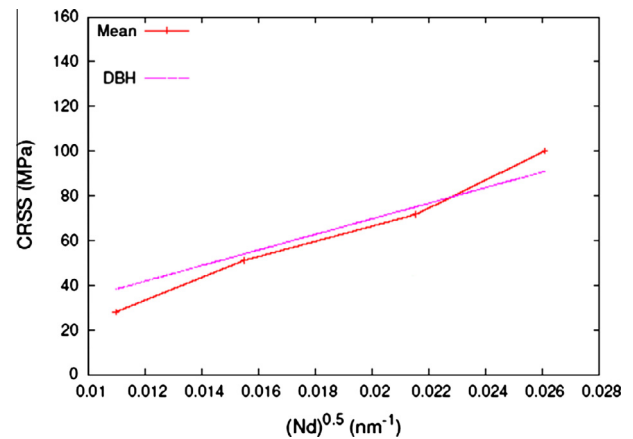

Fig. 5. Comparison of mean simulated and analytically predicted values for CRSS as a function of $\sqrt{Nd}$.

Fig. 4. Contour plot of the elastic interaction energy density field of an $\langle a_2 \rangle$ damage loop, resolved on the glide plane. This slice was taken approximately 7 nm above the center of the damage loop (along *X*-axis direction).
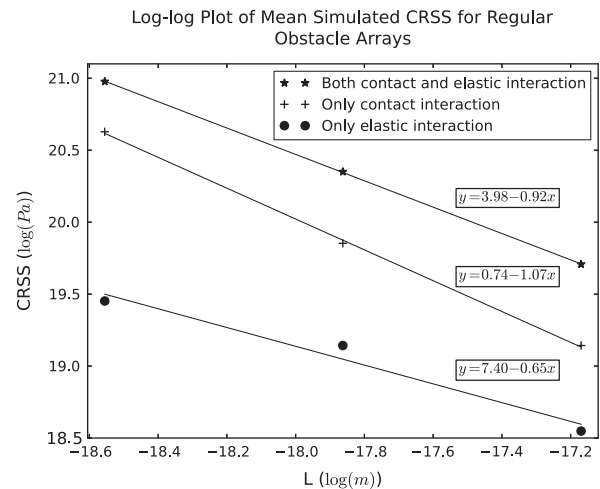

Fig. 6. Plots of log (CRSS) vs. log (*L*) for regular arrays of $\langle a_3 \rangle$ -type damage loops (see Tables 1 and 2). Straight lines were fitted to the data points (solid lines and printed equations). For the cases when contact interactions were considered, it is found that mean CRSS is approximately $\propto L^{-1}$ (fitted coefficients of 0.92 and 1.07) – indicating the scaling with respect to obstacle spacing appears close to what si predicted by the Orowan equation. In contrast, when only elastic interaction is considered, the fitted exponent is not close to −1 (fitted coefficient of 0.65).
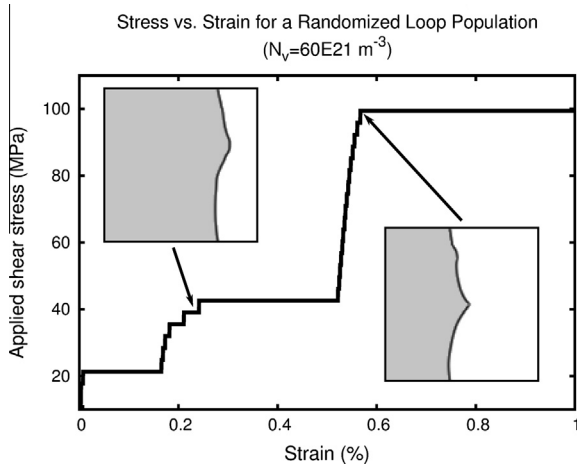
Fig. 7. Typical stress versus strain curve produced by a simulation with a population of damage loops having $N = 60E21$ m^{-3}. Insets show the disposition of the η field just prior to critical stress increases. The earlier inset shows the dislocation pinned by a strong elastic interaction, and the later inset shows the dislocation simultaneously pinned by a sessile jog and a strong elastic interaction.

Table 3
CRSS results for population simulations.

N ($\times 10^{21}$ m^{-3})	11	22	41	60
#1	28.4	74.6	71.0	78.1
#2	78.1	32.0	95.9	60.4
#3	74.6	78.1	81.7	120.7
#4	28.4	32.0	113.6	99.4
#5	39.1	71.0	88.7	166.9
#6	24.9	81.7	56.8	106.5
#7	71.0	85.2	103.0	138.5
#8	24.9	67.5	81.7	159.8
#9	24.9	56.8	95.9	81.7
#10	28.4	74.6	71.0	131.4
Mean (Std. Dev)	42.3(22.7)	65.3(19.2)	85.9(17.0)	114.3(35.5)

A typical stress versus strain curve obtained from a simulation with a population of damage loops is shown in Fig. 7. Stress versus strain curves are generated by plotting instantaneous strain against applied stress – horizontal line segments indicate periods of easy penetration at a given applied stress, while vertical steps indicate increases in stress after pinning. Individual CRSS values for each simulation and the resulting population means are summarized in Table 3. Because of the random nature of damage loop spatial arrangement, there is significant scatter in the results at each number density.

4. Discussion

4.1. Regular arrays

From our simulations of regular arrays of damage loops, it is clear that long-range elastic interactions provide a significant contribution to the overall hardening effect. As measured by the Orowan hardening relation, the addition of the damage loop's stress field increased obstacle strength α from 0.79 to 1.17, while the stress field alone produced hardening that was at least of the same order of magnitude as the contact interactions. In light of these results, simply ignoring or neglecting the long-range elastic interactions between glide dislocations and damage loops seems inappropriate.

When both contact interactions and damage loop stress fields are considered, we found that the relationship between hardening and obstacle spacing is not appreciably altered from the predic-

tions of Orowan hardening; log–log plots of these data show that CRSS is still proportional to L^{-1} (Fig. 6). Therefore, while elastic interactions significantly increased the effective obstacle strength of the loop, it does not change the Orowan hardening mechanism. When only elastic interaction was considered we found that the CRSS does not follow the same trend with respect to spacing. The log–log plots show that the CRSS is no longer proportional to L^{-1}. This is perhaps not surprising when the nature of the obstacle is considered. The magnitude and shape of the elastic interaction fields are strongly dependent on damage loop spacing, which in turn means that the obstacle strength of the damage loop is a function of spacing. In contrast the Orowan hardening law was derived assuming that both α and particle size/shape are constants. That CRSS was $\propto L^{-1}$ when both contact pinning and damage loop stress were active is due to the dominance of the contact interaction hardening at the simulated values of L. Some attempts have been made to consider the contribution of hardening due to stress fields, in the context of precipitation hardening [26]. As reviewed by Ardell, however, these methods have demonstrated limited success [26]; the nature of long-range elastic interaction makes it difficult to capture analytically. Rather, if accuracy is required then numerical techniques (such as those employed in this study) are called for.

4.2. Random arrays

Simulations of random arrays of damage loops resulted in a range of CRSS values for each number density, as may be seen in Table 3. Previous computational investigations of obstacle hardening have typically measured the maximum CRSS found in a single simulation containing many obstacles, and taken this as representative for the obstacle population being tested (see, e.g. the description of Foreman and Makin's procedure [27]). Rather than adopt this approach, we have performed multiple independent simulations, and reported the mean CRSS, in addition to individual (and extreme) values for each number density. This choice was driven both by memory-driven limitations on simulation size and by a desire to better characterize the spatial variation of local CRSS which might exist in a macroscopic sample.

In order to compare our results to DBH analytical predictions we will analyze the simulated CRSS with respect to $\sqrt{Nd}$. Different effective spacings may be derived (e.g. from stereological considerations [26]), but this approximate square lattice spacing of a random obstacle distribution has typically been used in analytical prediction of irradiation hardening [22]. When Eq. (1) was fitted to the mean CRSS data (see Table 4), we found $\alpha = 0.37$. The agreement between this fit and the simulated mean CRSS values is reasonable, given the range of the standard deviations in CRSS. In Fig. 5, we plot the simulated mean, maximum and minimum values of CRSS against $\sqrt{Nd}$. The DBH theory predicts a linear relationship (i.e. $\tau \propto N^{1/2}$); the mean CRSS results from our simulations fit

Table 4
Comparison of CRSS increments derived from the mean CRSS of population simulations with the analytical predictions of simple dispersed barrier hardening models. The value of $\alpha = 0.5$ given by Was for damage loops formed during irradiation [21]. The mean damage loop diameter for these simulations was $\bar{d} = 11 nm$. In the third column, the obstacle strength parameter α was fitted via least-squares fitting to the simulation mean values – finding $\alpha = 0.37$.

N ($\times 10^{21}$ m^{-3})	$\Delta\tau = 0.5\mu b\sqrt{N\bar{d}}$ (MPa)	$\Delta\tau = 0.37\mu b\sqrt{N\bar{d}}$ (MPa)	Sim. mean $\Delta\tau$ (MPa)
11	53.1	38.2	28.1 ± 22.7
22	75.1	54.0	51.1 ± 19.2
41	104.4	75.1	85.9 ± 17.0
60	126.4	91.0	100.1 ± 35.5

to $\tau \propto N^n$, with a value of $n \approx 0.57 \pm 0.03$. We believe that this could be attributed to the fact that the CRSS is determined by both pinning contact interactions and the stress fields of the damage loops, rather than by the contact interaction alone.

When considering a spatially randomly distributed population of multiple obstacle types, the CRSS may be determined via a rule of mixtures (e.g. the Pythagorean sum, $\tau^2 = \tau_a^2 + \tau_b^2$, where τ is the total CRSS, and τ_i is the CRSS of the ith obstacle population by itself) [26,34]. If either of the component CRSS values has any dependence on N other than $\propto N^{1/2}$, then the τ vs $\sqrt{Nd}$ trend will be non-linear. As shown in Section 4.1, hardening due to pure elastic obstacles is not proportional to L^{-1}, and the contribution of elastic obstacles seems to be a likely cause of the curvatures observed in Fig. 5, as well as the trend in CRSS observed by Li et al. (who also considered the stress fields of damage loops) Li et. al. [39].

The distribution of CRSS values is due to the effects of non-uniform spatial distribution. The minimum values are determined by the weakest obstacles: long-range elastic interaction with damage loops distant from the slip plane. In these case the obstacles and pinned glide dislocation configurations are quite different from those in the classic Orowan hardening mechanism. Nanometer scale regions of repulsive elastic interaction occur, resulting in shallow bowing of the gliding dislocation. The mean CRSS increases with N, due to increasing overlap of damage loop stress fields and increasing pinning junctions.

4.3. Yield stress estimation

Finally, in order to compare our results with experimental measurements of irradiation hardening, we conduct a rudimentary Schmid factor analysis. The Schmid factor for a tensile test of a single crystal is classically defined as

$$\tau^{CRSS} = \sigma^y \cos(\phi)\cos(\lambda)$$

where ϕ is the angle between the tensile axis and the slip plane normal, λ is the angle between the tensile axis and the slip directions and $m = \cos(\phi)\cos(\lambda)$ is the Schmid factor. Since most mechanical tests are conducted with polycrystalline samples machined from fuel cladding or pressure tubes, some assumptions regarding the predominant texture are necessary to extrapolate from our single-plane simulations. Himbeault et al. characterized the idealized texture of as-formed pressure tubes as having the $\langle 0001 \rangle$ direction aligned with the tube's transverse direction, $\langle 11\bar{2}0 \rangle$ with the radial, and $\langle 10\bar{1}0 \rangle$ with the longitudinal [11]. In this perfect orientation, there is no resolved shear stress on the simulated prismatic system – suggesting that these tubes are typically poorly oriented for prismatic slip. From Himbeault's pole figures, we can estimate a typical range of deviation from this orientation. The basal axis was found to be widely distributed between the radial and transverse directions, with very little deviation toward the longitudinal. The $\langle 10\bar{1}0 \rangle$ axis deviates less in magnitude than the basal, but evenly towards the radial and transverse. Based on these observations, we have for transverse loading $0° \leqslant \lambda \leqslant 40°$ and $70° \leqslant \phi \leqslant 90°$, and for longitudinal loading we have $70° \leqslant \lambda \leqslant 90°$ and $0° \leqslant \phi \leqslant 20°$. These values in turn yield $0 \leqslant m^{trans} \leqslant 0.26$ and $0 \leqslant m^{long} \leqslant 0.32$.

Comparison with experimentally measured yield stresses and Schmid factor based extrapolations from our simulation are made in Table 5 and we find good agreement between the two. This suggests that our model is able to provide a reasonable estimate of irradiation hardening in Zr. Detailed comparison is not possible, given the simplified nature of our yield strength analysis. Properly, a Taylor factor analysis or a full crystal plasticity model (such as the one developed in [24]) is necessary to extrapolate from our CRSS calculations to a polycrystalline yield stress (the Schmid factor is only accurate for single crystals).

Table 5
Comparison of yield strength increment values from literature with those derived in this work.

References	$\Delta\sigma^y$ (MPa)
This work (m^{long} = 0.32)	88–313
This work (m^{trans} = 0.26)	108–385
Davies et al. [16]	224
Morize et al. [67]	210–235
Onimus et al. [62]	150–365
Fregonese et al. [68]	170

4.4. Future work

Without modification of the model, further study is also possible regarding the effect of statistical variation in damage loop size and $\vec{b}$, as well as their spatial ordering (such as the often observed "rafting" along the basal plane). With some modifications, CRSS values for slip systems besides the prismatic slip could also be predicted. Furthermore, with input from more detailed atomistic modeling of glide dislocation and damage loop interactions, the contact interaction model could be improved. In particular, the simplified sessile junction assumptions employed in this work may be expanded by incorporating explicit junction strengths as a function of the character of the glide dislocation and the relative orientation of the damage loops [61,69–71]. Naively, this could be achieved by assigning junction strengths to the randomly created loop population, then explicitly calculating the glide force being exerted on the junction at each point in simulation time. A more sophisticated approach may be to treat sessile junctions as energetically favorable configurations, directly via the free energy functional. The present work may also be coupled with models of damage loop growth and dissolution, relaxing the assumption that damage loops do not evolve. Finally, the CRSS output from the model could be employed as input for a more realistic crystal plasticity model rather than the simple Schmid factor analysis we have used.

5. Conclusions

We studied irradiation hardening in pure zirconium by computer simulations using the phase field method. Various populations of damage loops were constructed according to experimental observations.

Long range elastic interactions between damage loops and glide dislocations were incorporated via phase field microelasticity theory, while a simple implementation of Dispersed Barrier Hardening was employed to incorporate contact interactions. The long-range elastic interactions were found to contribute significantly to hardening. In the case of regular arrays of loops, elastic interactions were found to increase the obstacle strength of the jog "particles" from $\alpha = 0.79$ to $\alpha = 1.17$. In the case of randomly spatially distributed damage loops, in particular at large number densities, the elastic interactions resulted in a non-linear dependance of CRSS on $\sqrt{Nd}$, which renders analytical models of irradiation hardening less accurate. Finally, a simplistic Schmid factor analysis was performed to connect simulated CRSS values with experimentally measured yield stresses, with good agreement being found between the two.

References

[1] M. Griffiths, Journal of Nuclear Materials 159 (1988) 190–218.
[2] D. Northwood, Journal of Nuclear Materials 79 (1979) 379–394.
[3] C. Lemaignan, Comprehensive Nuclear Materials, vol. 2, Elsevier, pp. 217–232.
[4] X. Zu, K. Sun, M. Atzmon, L. Wang, L. You, F. Wan, J. Busby, G. Was, R. Adamson, Philosophical Magazine 85 (2005) 649–659.

[5] F. Onimus, J. Bechade, Comprehensive Nuclear Materials, vol. 4, Elsevier, pp. 1–31.
[6] L. Fournier, A. Serres, Q. Auzoux, D. Leboulch, G. Was, Journal of Nuclear Materials 384 (2009) 38–47.
[7] R. Gilbert, K. Farrell, C. Coleman, Journal of Nuclear Materials 84 (1979) 137–148.
[8] C. Regnard, B. Verhaeghe, F. Lefebvre-Joud, C. Lemaignan, in: Zirconium in the Nuclear Industry: 13th International Symposium.
[9] P. Kelly, R. Blake, Philosophical Magazine 28 (1973) 415–426.
[10] M. Griffiths, Philosophical Magazine A 63 (1991) 835.
[11] D.D. Himbeault, C.K. Chow, M.P. Puls, Metallurgical and Materials Transactions A 25 (1994) 135–145.
[12] M.L. Saux, J. Besson, S. Carassou, C. Poussard, X. Averty, Journal of Nuclear Materials 378 (2008) 60–69.
[13] F. Onimus, J. Bechade, C. Duguay, D. Gilbon, P. Pilvin, Journal of Nuclear Materials 358 (2006) 176–189.
[14] F. Onimus, I. Monnet, J.L. Bechade, C. Prioul, P. Pilvin, Journal of Nuclear Materials 328 (2004) 165–179.
[15] T. Torimaru, M. Nakatsuka, T. Yasuda, Journal of Nuclear Materials 238 (1996) 169–174.
[16] P. Davies, R. Hosbons, M. Griffiths, C. Chow, ASTM, Baltimore, MD, 1993, pp. 135–166.
[17] T.S. Byun, K. Farrell, Journal of Nuclear Materials 326 (2004) 86–96.
[18] F. Onimus, J. Bechade, Journal of Nuclear Materials 384 (2009) 163–174.
[19] R.L. Fleischer, Acta Metallurgica 11 (1963) 203–209.
[20] B.N. Singh, A.J.E. Foreman, H. Trinkaus, Journal of Nuclear Materials 249 (1997) 103–115.
[21] G. Was, Fundamentals of Radiation Materials Science, Springer-Verlag, Berlin, 2007.
[22] R.E. Stoller, S.J. Zinkle, Journal of Nuclear Materials 283–287 (2000) 349–352.
[23] R. Chaouadi, T. Hirai, J. Linke, G. Pintsuk, Journal of Nuclear Materials 386–388 (2009) 544–549.
[24] C. Deo, C. Tome, R. Lebensohn, S. Maloy, Journal of Nuclear Materials 377 (2008) 136–140.
[25] A. Arsenlis, B.D. Wirth, M. Rhee, Philosophical Magazine 84 (2004) 3617.
[26] A.J. Ardell, Metallurgical Transactions A 16 (1985) 2131–2165.
[27] A.J.E. Foreman, M.J. Makin, Philosophical Magazine 14 (1966) 911.
[28] J.W. Morris, D.H. Klahn, Journal of Applied Physics 44 (1973) 4882–4890.
[29] J. Nie, B. Muddle, Acta Materialia 56 (2008) 3490–3501.
[30] S. Weakley-Bollin, W. Donlon, W. Donlon, C. Wolverton, J. Allison, J. Jones, Metallurgical and Materials Transactions A 35 (2004) 2407–2418.
[31] A.W. Zhu, A. Csontos, E.A. Starke, Acta Materialia 47 (1999) 1713–1721.
[32] A.W. Zhu, E.A. Starke, Acta Materialia 47 (1999) 3263–3269.
[33] G. Monnet, Philosophical Magazine 86 (2006) 5927–5941.
[34] S. Queyreau, G. Monnet, B. Devincre, Acta Materialia 58 (2010) 5586–5595.
[35] G. Adjanor, S. Bugat, C. Domain, A. Barbu, Journal of Nuclear Materials 406 (2010) 175–186.
[36] S. Jumel, J.V. Duysen, J. Ruste, C. Domain, Journal of Nuclear Materials 346 (2005) 79–97.
[37] T. Nogaret, D. Rodney, M. Fivel, C. Robertson, Journal of Nuclear Materials 380 (2008) 22–29.
[38] A. Luft, Progress in Materials Science 35 (1991) 97–204.
[39] D. Li, H. Zbib, H. Garmestani, X. Sun, M. Khaleel, Computational Materials Science 50 (2011) 2496–2501.
[40] D. Bacon, Y. Osetsky, Materials Science and Engineering A 400-401 (2005) 353–361.
[41] N.D. Diego, Y. Osetsky, D. Bacon, Journal of Nuclear Materials 374 (2008) 87–94.
[42] T.D. de la Rubia, H.M. Zbib, T.A. Khraishi, B.D. Wirth, M. Victoria, M.J. Caturla, Nature 406 (2000) 871–874.
[43] V. Dubinko, A. Turkin, A. Abyzov, M. Griffiths, Zirconium in the Nuclear Industry: 14th International Symposium 1467 (2005) 157–174.
[44] R. Voskoboinikov, Y. Osetsky, D. Bacon, Materials Science and Engineering A 400-401 (2005) 49–53.
[45] R. Voskoboynikov, Y. Osetsky, D. Bacon, Materials Science and Engineering A 400-401 (2005) 54–58.
[46] J.S. Robach, I.M. Robertson, B.D. Wirth, A. Arsenlis, Philosophical Magazine 83 (2003) 955.
[47] D. Rodney, G. Martin, Physical Review Letters 82 (1999) 3272–3275.
[48] B. Wirth, V. Bulatov, T. Diaz de la Rubia, Journal of Eengineering Materials and Technology 124 (2002) 329–334.
[49] A. Khachaturyan, Theory of Structural Transformations in Solids, John Wiley & Sons, New York, 1983.
[50] Y.U. Wang, Y.M. Jin, A. Cuitino, A.G. Khachaturyan, Acta Materialia 49 (2001) 1847–1857.
[51] C. Shen, Y. Wang, Acta Materialia 51 (2003) 2595–2610.
[52] C. Shen, Y. Wang, Acta Materialia 52 (2004) 683–691.
[53] V. Vitek, Philosophical Magazine 18 (1968) 773.
[54] G. Monnet, B. Devincre, L. Kubin, Acta Materialia 52 (2004) 4317–4328.
[55] D. Hull, Introduction to Dislocations, 2nd ed., Pergammon Press, Oxford, 1975.
[56] G. Carpenter, Scripta Metallurgica 10 (1976) 411–413.
[57] J. Hirth, Journal of Applied Physics 32 (1961) 700–706.
[58] R. Madec, B. Devincre, L. Kubin, Physical Review Letters 89 (2002) 255508.
[59] F. Onimus, L. Dupuy, F. Mompiou, Progress in Nuclear Energy 57 (2012) 77–85.
[60] B. Devincre, L. Kubin, T. Hoc, Scripta Materialia 54 (2006) 741–746.
[61] L. Wickham, K. Schwarz, J. Stölken, Physical Review Letters 83 (1999) 4574–4577.
[62] F. Onimus, J. Bechade, C. Prioul, P. Pilvin, I. Monnet, S. Doriot, B. Verhaeghe, D. Gilbon, L. Robert, L. Legras, J. Mardon, ASTM STP, vol. 1467, American Soceity for Testing and Materials, Stockholm, Sweeden, 2004, pp. 53–78.
[63] G. Simmons, H. Wang, Single Crystal Elastic Constants and Calculated Aggregate Properties, MIT Press, Cambridge, MA, 1971.
[64] H. Khater, D. Bacon, Acta Materialia 58 (2010) 2978–2987.
[65] A. Kelly, R. Nicholson, Strengthening Methods in Crystals, Applied Science Publishers Ltd., London,UK, 1971.
[66] N. Zhou, Simulation study of directional coarsening (rafting) of gamma prime in single crystal Ni–Al, Ph.D. thesis, The Ohio State University, Columbus, OH, 2008.
[67] P. Morize, J. Baicry, J. Mardon, ASTM STP, vol. 939, American Society for Testing and Materials, Strasbourg, France, 1987, pp. 101–119.
[68] M. Fregonese, C. Regnard, L. Rouillon, T. Magnin, F. Lefebvre, C. Lemaignan, ASTM STP, vol. 1354, American Soceity for Testing and Materials, Toronto, Canada, 2000, pp. 377–398.
[69] V. Shenoy, R. Kukta, R. Phillips, Physical Review Letters 84 (2000) 1491–1494.
[70] G. Schoeck, R. Frydman, Physica Status Solidi (b) 53 (2006) 661–673.
[71] T. Nogaret, C. Robertson, D. Rodney, Philosophical Magazine 87 (2007) 945–966.